

pubs.acs.org/JPCC Article

Differential Diffuse Reflectance Spectral Calculation of Crystalline Composition and Bandgap Energy in Metal Oxides Mixtures

Published as part of The Journal of Physical Chemistry C special issue "Spectroscopic Techniques for Renewable Energy".

Thu D. Nguyen, Chenfeng Huang, George Tsilomelekis, and Fuat E. Celik*



Cite This: https://doi.org/10.1021/acs.jpcc.4c03763



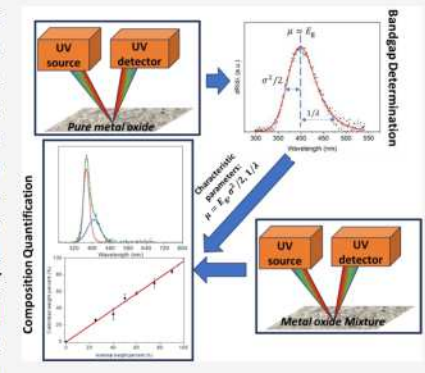
ACCESS

Metrics & More

Article Recommendations

s Supporting Information

ABSTRACT: Mixtures of metal oxides pose unique challenges for independent measurement of bandgap energies of each phase present. A facile technique with such a capability that can also determine the composition of the mixture would be of interest in industrial applications and academic research. UV—vis spectroscopy has several benefits among characterization techniques, including fast data collection, short training time for users, including safety training, and the ability to perform consistent quantitative analysis in continuous operation. Here we modify the derivative peak fitting of the diffuse reflectance UV—vis spectroscopy (DPR) technique by implementing the exponentially modified Gaussian (EMG) as a fitting model. With EMG, the applicability of the DPR method was extended to additional metal oxides, including all three common phases of titania and other semiconducting metal oxides commonly used in catalysis and photocatalysis: CeO₂, ZnO, SnO₂, V₂O₅, MoO₃, Y₂O₃, Ta₂O₅, and Nb₂O₅. This is due to the similarity between the distribution of electronic excitation by the UV—vis photon



and the EMG function. Using EMG, the DPR method was used to calculate the "effective" bandgap energy of each metal oxide phase in binary and ternary mixtures of powders and to quantify phase composition. A response factor for each metal oxide studied relative to anatase ${\rm TiO}_2$ is reported as a calibration method and demonstrated to be reusable, even in ternary mixtures.

1. INTRODUCTION

Metal oxides are one of the most essential classes of heterogeneous catalysts for a wide range of chemical processes, applied in refining, petrochemical, and photocatalytic processes. Early transitional metal oxides such as vanadia (V2O5), niobia (Nb₂O₅), tantalum oxide, and molybdena (MoO₃) have useful redox properties for oxidative reactions. 1-6 Metal oxides with strong Lewis acid sites such as molybdenum oxide and tungsten oxide (WO3) are useful in dehydration reactions. Despite their lack of strong reactivity in conventional chemical reactions, titanium oxide (TiO2) and cerium oxide are thermally stable and can be synthesized to achieve a tunable morphology, small crystallite structures, and high surface area. 7,8 As a result, these metal oxides are commonly used as metal oxide supports in many catalyst systems. In the field of photocatalysis, semiconducting metal oxides such as titanium oxide, zinc oxide, and cerium oxide have emerged as promising materials because of their narrow bandgap.9-11 Many candidates in this oxide class not only performed interesting chemical or physical properties but also are generally benign to both the environment and human health and thus have been gaining even more interest in academic and industrial research.

The significant role of metal oxides has led to numerous studies regarding characterization techniques by which the intrinsic structural properties of these oxides could be effectively determined and distinguished. Of the available characterization techniques for solids, UV—vis spectroscopy has provided a great insight into general electronic structures of materials through their electronic excitation phenomena. The position of an absorption band from UV—vis spectra can be utilized to obtain information about the electronic structure of solid compositional phases. This information can be used to identify the presence of metals or metal oxides and their oxidation states in the solid phase. Among the important features of metal oxides provided by UV—vis spectroscopy are the band edge positions of the conduction and valence bands, as well as the bandgap energy between them, which are of great interest for electrical, electronic, and photocatalytic applications.

A simple analysis technique for diffuse reflectance UV-vis spectra was developed and justified by Tauc to estimate the

Received: June 5, 2024 Revised: September 18, 2024 Accepted: September 20, 2024



bandgap energy for thin film semiconductors. 12 Although this method is applicable in the case of many semiconductor powders, several evident limitations can be recognized. Not all the required assumptions of the method may hold for semiconductor powders prepared with complex composition or morphology. While bandgap energy values for the common polymorphs of TiO₂ anatase and rutile have been determined with general consensus to be 3.20 and 3.03 eV, 13,14 respectively, reported bandgap energies of other metal oxide powders show variation. This deviation may arise from the effect of synthesis methods, which result in different morphologies or particle sizes. However, the bandgap variation from the Tauc analysis method could also be a result of the subjectivity when applying the method. Moreover, since the Tauc method was originally devised for thin films comprising a single pure material phase, the method is unable to distinguish individual bandgap energies of each component solid in a mixture, giving only a single apparent overall value instead.

We introduced derivative peak fitting of diffuse reflectance spectra analysis (DPR) as an alternative method in the determination of bandgap energy of semiconductor mixtures. 1 Implementation of this method on anatase and rutile polymorphs of titania powder exemplified the advantage of the method in reducing the subjective error and experimental deviation. Likewise, it was illustrated that when anatase and rutile phases were mixed, the DPR method could not only effectively identify the presence of each phase but also quantify the compositional phase of this mixture, in both ex-situ and insitu conditions, while also reporting the bandgap energies of the anatase and rutile phases independently. 18 Measuring the bandgap energies of each phase in well-known mixtures of anatase and rutile such as P25 is otherwise a challenging task, with many reports citing just a single "combined" bandgap energy instead, with little connection to the actual electronic structure of the underlying materials.

Acknowledging the significant role of metal oxides in many fields of relevance in renewable and alternative energy and the necessity for quick and accurate electronic structure characterization as well as compositional quantification for this class of materials, the main objective of this work was to demonstrate the broad applicability of the DPR method by studying more semiconducting metal oxides and relevant mixtures, including brookite TiO2, CeO2, ZnO, SnO2, V2O5, MoO3, Y2O3, Ta2O5, and Nb2O5. This was accomplished by introducing the exponentially modified Gaussian (EMG) fitting function, which is a better fit to the distribution of electronic states in all metal oxides compared to the Gaussian fits used previously. A set of calibration coefficients of various metal oxides relative to anatase TiO2, which are intrinsic properties of each material, is provided to quantify these semiconductors in any given UV-vis spectrometer.

2. EXPERIMENTAL METHODS

2.1. Materials and Sample Preparation. Powdered metal oxide materials were obtained from Thermo Fisher, including anatase ${\rm TiO_2}$ (AA3995314), rutile ${\rm TiO_2}$ (AC270461000), brookite ${\rm TiO_2}$ (50-186-2498), ${\rm CeO_2}$ (AA12925A3), ${\rm ZnO}$ (AAA161880I), ${\rm SnO_2}$ (AA12283A3), ${\rm V_2O_5}$ (AA11093A1), ${\rm MoO_3}$ (AA3668736), ${\rm Y_2O_3}$ (AA4428618), ${\rm Ta_2O_5}$ (AA1470918), ${\rm Nb_2O_5}$ (AA11365A3), and ${\rm CuO}$ (AC405860250). Degussa P25 ${\rm TiO_2}$ (Lot: 613020598) was obtained from Evonik. Binary and ternary mixtures of these powdered metal oxides were made by using

nominal weight percentages. Each pure material was ground mildly with an agate mortar and pestle to achieve similar agglomerate particle sizes. Mixtures were prepared from ground pure materials and stored in 10 mL vials with the total mass of each mixture to be approximately 5–7 g. Mixtures in the vials are then mixed using a vortex mixer, Vortex Genie 2, under Touch Mode at fixed power level 5 for approximately 10 min to produce a homogeneous composition distribution in the powder.

2.2. UV—Visible Spectroscopy. Samples were loosely loaded into a 0.022 mL micro sample cup for spectral analysis, and excess powder was scraped off to ensure a filled sample cup and a flat surface. Diffuse reflectance UV—visible spectroscopy was carried out on a Thermo Scientific Evolution 3000 spectrophotometer equipped with a Harrick Scientific Praying Mantis diffuse reflectance accessory. Spectra were scanned between 190 and 1100 nm in intervals of either 0.5 or 2.0 nm. The absolute reflectance standard was collected using a Spectralon disk.

2.3. Derivative Peak Fitting of Diffuse Reflectance Spectra. In this study, raw data in the form of absolute reflectance R_{∞} was used to calculated spectral intensity as the derivative $\frac{dR_{\infty}}{d\lambda}$ of absolute reflectance with respect to wavelength λ (nm)

$$\frac{\mathrm{d}R_{\infty}}{\mathrm{d}\lambda} = \frac{R_{\infty_i} - R_{\infty_{i+1}}}{\lambda_i - \lambda_{i+1}}$$

and then imported into Fityk software¹⁹ for peak deconvolution. The exponentially modified Gaussian distribution function was implemented as a fitting function. Preservation of physical meaning in the peak fitting procedure enforced the compliance of a fitting principle, in which each peak added into the function list should correspond to a component semiconductor in the examined powder. Minimization of error by the Levenberg–Marquardt method was used for the fitting process. Peak characteristics, including peak position, half-width at half-maximum, and skewness, were used for phase identification. The peak position corresponds to the bandgap energy of a given material.

The area under an obtained deconvoluted peak could be considered as a representation of the total amount of excited electrons from a specific component phase in the oxide. In other words, the component peak area has a strong correlation with the mass fraction of component oxide in a mixture. It is reasonable to assume that each oxide phase would respond distinctly, thus exhibiting an intrinsic absolute response factor (ARF). Although this intrinsic absolute response factor could not be determined individually, the ratio of ARFs from 2 materials could still be determined and utilized in compositional phase determination, as shown in the equation

$$\begin{split} &\frac{\text{wt \%}_{A}}{100} = \frac{\text{mol}_{A} \cdot \text{MW}_{A}}{\text{mol}_{A} \cdot \text{MW}_{A} + \text{mol}_{B} \cdot \text{MW}_{B}} \\ &= \frac{\frac{PA_{B}}{ARF_{A}} MW_{A}}{\frac{PA_{A}}{ARF_{A}} MW_{A} + \frac{PA_{B}}{ARF_{B}} MW_{B}} \\ &= \frac{PA_{A} \cdot RRF \cdot MW_{A}}{PA_{A} \cdot RRF \cdot MW_{A} + PA_{B} \cdot MW_{B}} \end{split}$$

where wt % is the weight percentage of corresponding component, PA is the peak area under the curve representing corresponding component, MW is the molecular weight of the corresponding component, ARF and RRF are the absolute and relative responding factor of the components in the mixture, and A, B represent the component metal oxides in a binary mixture. From this argument, calibration lines were constructed by utilizing the concept of binary relative response factors (RRF). The RRF $\left(=\frac{ARF_B}{ARF_A}\right)$ for each binary mixture was determined through linear regression in which R^2 was maximized.

3. RESULTS AND DISCUSSION

3.1. Revision of Tauc Method. As first reported by Urbach, 21 many crystalline metal oxides exhibit an exponential

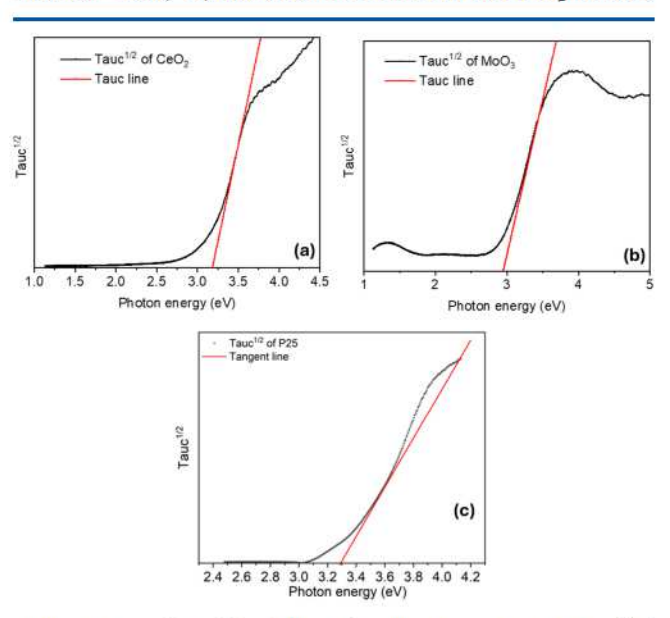


Figure 1. Tauc plot of the diffuse reflectance UV—vis spectrum of (a) pure cerium oxide, (b) molybdenum oxide, and (c) P25, using r=1/2 for a direct allowed transition. The Tauc line, determining the bandgap energy position of (a) 3.18, (b) 2.95, and (c) 3.3 eV. As P25 is a mixture of metal oxides, the Tauc method gives only a single bandgap energy.

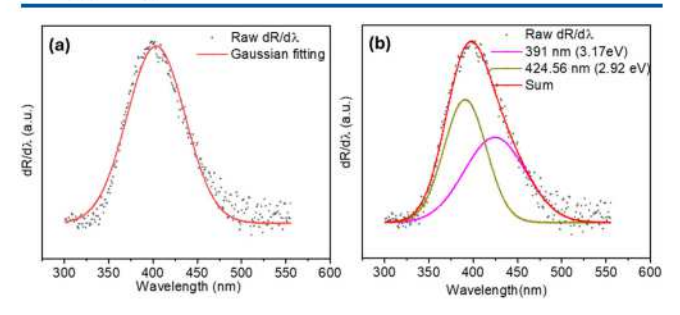


Figure 2. (a) Fitting one Gaussian function to the derivative spectrum of cerium oxide. The peak center is at 405 nm (3.06 eV). (b) Fitting two Gaussian functions to the derivative spectrum of cerium oxide

increase in light absorption with photon energy near their absorption edge. Some theoretical models^{22–25} have been developed to fit experimental data and gain a conceptual understanding of this so-called Urbach tail of the absorption coefficient α , which was cast in the form

$$\alpha = A \exp[\sigma(\hbar\omega - \hbar\omega_0)/k_BT]$$

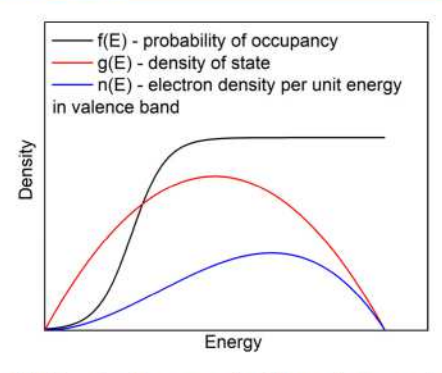


Figure 3. Carrier density as a function of energy in a typical semiconductor. The electron density n(E) is the product of both the probability of occupancy f(E) and the density of states g(E), leading to a typical skewed distribution function.

where $\hbar\omega$ is the photon energy, $k_{\rm B}$ is the Boltzmann constant, T is the temperature, A and $\hbar\omega_0$ are constants, and σ is a measure of the absorption curve's steepness.

Complex contributions to the shape of the Urbach tail were attributed^{26,27} to disordering due to temperature, structure, and composition. These distortions manipulate the distribution of density of states (DOS) at the tail of the valence band and electrons located within this region, giving rise to diverse shapes of absorption spectra.

It was observed by $Tauc^{12}$ that the absorption tail of thin film amorphous germanium exhibited Gaussian behavior, which was interpreted as the excitation of electrons within localized states rather than the transition between valence and conduction band. This interpretation implies that the onset of absorption from the excitation measurement should not be taken as the bandgap energy. Assuming band structure follows parabolic shapes and has extrema at the Γ point of the Brillouin zone, the scale of absorption represented by the imaginary part of the dielectric coefficient ε_2 in the regime of bandgap energy $(E_{\rm e})$ could be obtained as

$$\omega^2 \varepsilon_2 \sim (\hbar \omega - E_{\rm g})^2$$

From this scaling, determination of minimum direct transition between valence band and conduction band was methodized by plotting $(\hbar\omega\alpha)^{1/2}$ versus $\hbar\omega$, in which α is the absorption coefficient, and finding the *y*-interception of tangent line of $(\hbar\omega\alpha)^{1/2}$. The Tauc method was also extended for allowed indirect transition²⁸ and other types of transitions^{29,30} by modifying the scaling of $\hbar\omega\alpha$ in order to identify the linear region of $(\hbar\omega\alpha)^{1/n}$.

In this work, the representation of $(\hbar\omega\alpha)^{1/n}$, Tauc^{1/n}(E), was calculated as a scale of the product of the Kubelka–Munk function $F(R_{\infty})$ and its corresponding photon energy $E(\lambda)$.

$$Tauc^{1/n}(E) = (F(R_{\infty})E(\lambda))^{1/n}$$

The touching point of the tangent line and $\mathrm{Tauc}^{1/n}(E)$ was found by locating the maximum of numerical $\frac{\mathrm{d}(\mathrm{Tauc}^{1/n}(E))}{\mathrm{d}E}$, which can be calculated as

$$\frac{d(\operatorname{Tauc}^{1/n}(E))}{dE} = \frac{(F(R_{\infty})E(\lambda))^{1/n_{i+1}} - (F(R_{\infty})E(\lambda))^{1/n_i}}{E_{i+1} - E_i}$$

where $F(R)_i$ and E_i represent the Kubelka–Munk function and photon energy at wavelength i.

Table 1. EMG Peak Parameters of Pure Materials

metal oxide	peak position (nm)	DPR BGE (eV)	Tauc BGE (eV)	ref BGE (eV)	HWHM of high-energy tail $(\sigma^2/2)$	RT of low-energy tail $(1/\lambda)$	skewness
TiO ₂ (anatase)	372	3.33	3.25	3.213,14	5.78	10.00	10.36
TiO ₂ (rutile)	400	3.09	3.14	3.03 ¹³	4.35	6.67	7.20
TiO ₂ (brookite)	364	3.41	3.33	3.27 ⁵⁵	3.94	12.50	63.86
CeO ₂	382	3.24	3.18	3.3656	11.6	33.33	47.46
ZnO	381	3.26	3.21	3.27 15,57 - 59	1.71	7.14	145.40
CuO	866	1.43	1.24	1.29 ^{60,61}	16.5	20.00	3.56
SnO_2	310	3.99	3.73	3.62, ⁶² 3.9 ⁶³	5.77	20.00	83.29
V_2O_5	518	2.4	2.23	2.4 ⁶⁴	9.9	20.00	16.49
MoO ₃	406	3.06	2.95	3.01-3.24, ³⁷ 3.14-3.34 ³⁸	14	1.00	0.00
Nb ₂ O ₅	396	3.13	3.02	$3.08 - 3.2^{65}$	6.42	11.11	10.37
Ta ₂ O ₅	305	4.06	3.91	3.9, ⁶⁶ 4 ⁶⁷	3.99	8.33	18.21
Y_2O_3	218	5.68	5.64	5.8, ⁶⁸ 6 ⁶⁹	1.44	2.50	10.17

Table 2. Parameters of Peak Deconvolution for Mixtures of Anatase TiO₂ and MoO₃

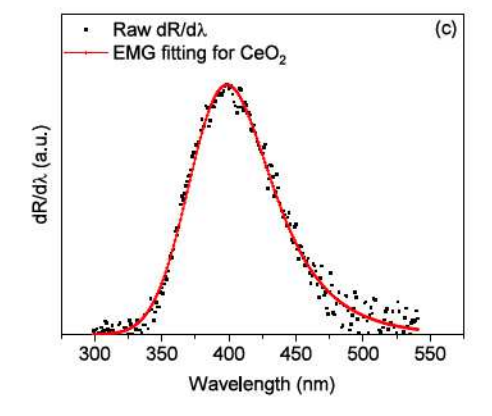
	μ (nm)		$\sigma^2/2$		1/2	
	anatase TiO ₂	MoO ₃	anatase TiO ₂	MoO ₃	anatase TiO ₂	MoO ₃
10% TiO ₂	363	405	4.65	14.2	10.0	1.00
25% TiO ₂	363	405	4.84	14.7	10.0	1.00
40% TiO ₂	366	405	5.25	14.4	10.0	1.00
50% TiO ₂	368	405	5.15	14.7	9.09	1.00
60% TiO ₂	368	405	5.15	13.6	9.01	1.00
75% TiO ₂	368	405	5.75	14.0	7.14	1.00
90% TiO ₂	368	405	5.75	14.0	8.33	1.00

Application of the Tauc method in determination of bandgap energy appears to be conveniently applicable without implementing cumbersome calculations; however, common semiconductors used in material industry do not strictly follow this approximation. In other words, the linear region on the curve of $(Tauc)^{1/n}$ is not always obviously observed. The pronounced manifestation of an Urbach tail on the absorption in the low energy tail significantly affects the shape of $(\hbar\omega\alpha)^{1/n}$

As shown in Figure 1a,b, the Tauc line could not perfectly touch the curve due to the Urbach effect. This difficulty hinders strict application, limiting the sensitivity of the Tauc method and potentially resulting in discrepancies in reported

bandgap energies. Such mismatch in the literature could be seen in a wide range of common used materials, such as amorphous silicon, 31,32 zinc oxide, $^{33-36}$ and molybdenum oxide.

3.2. Revision of Reported Stepwise Methods to Determine Bandgap Energy. In an attempt to amend the stepwise application of the Tauc method, Viezbicke 15 and then Coulter³⁹ suggested to linearize the Tauc curve in the region of band-to-band transition before fitting the tangent line. A new concept, dubbed as the near-edge absorptivity ratio (NEAR), was also introduced, which could then be used to evaluate the accuracy of determined bandgap and the contribution of subband excitation. This analysis procedure renders a justification in fitting a tangent line to the Tauc curve and results in a more consistent bandgap energy. Linearization, while narrowing down the deviation in bandgap energy determination, coincidentally removes absorption features when they are localized in the linearized regime. Even if the Tauc curve is not linearized, differences between single- and multiphase materials could hardly be captured using the Tauc method. This missing information can be seen in Figure 1c, in which bandgap energy obtained from Tauc analysis did not reflect the existence of two different phases of TiO2 in the material and could have led to a false interpretation that the long tail in the low-energy side was caused due to the Urbach effect as the crystalline structure was perturbed. Later on, recognizing the challenges in obtaining the bandgap energy for materials with multiple



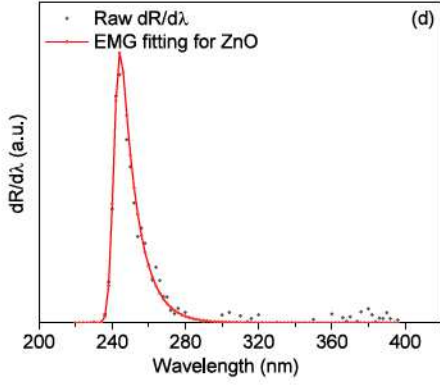


Figure 4. DPR with EMG fitting of some pure materials: (a) anatase TiO₂, (b) brookite TiO₂, (c) cerium oxide, and (d) zinc oxide. Parameters obtained are listed in Table 1.

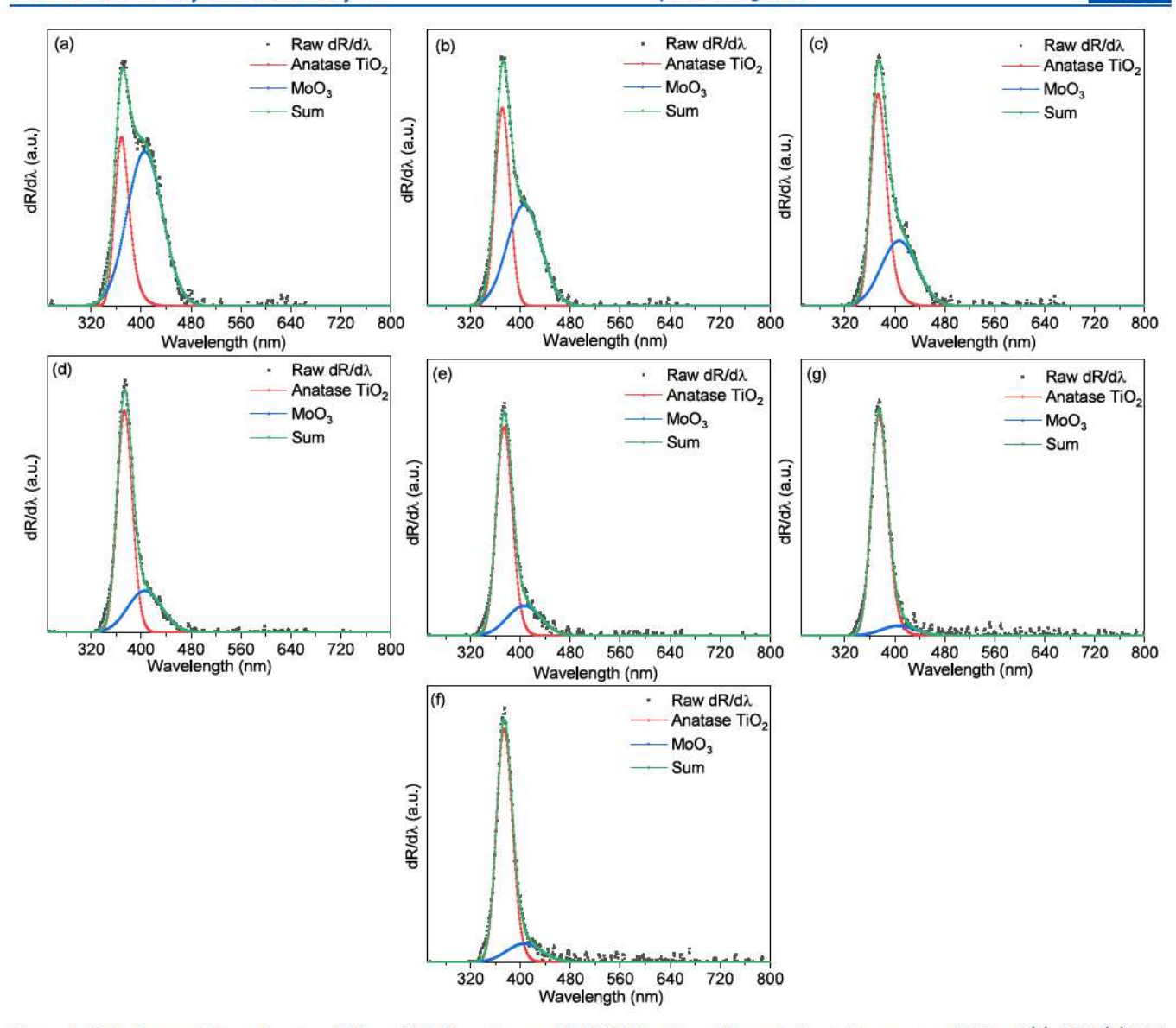


Figure 5. Peak deconvolution of anatase TiO₂ and MoO₃ mixtures with EMG function with nominal weight percents of TiO₂ of (a) 10%, (b) 25%, (c) 40%, (d) 50%, (e) 60%, (f) 75%, and (g) 90%.

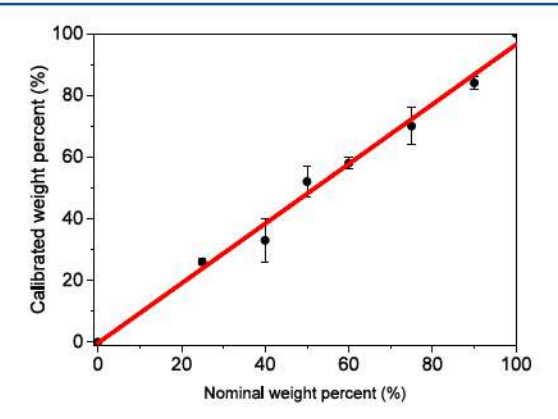


Figure 6. Calculated weight percentage, obtained from regressed RRF = 0.8, versus nominal weight percentage of anatase ${\rm TiO_2}$ in binary mixture with ${\rm MoO_3}$.

features such as P25, efforts were made by Welter et al. 17 to compare the consistency and accuracy of the linearization in the transition energy range of different commonly used

graphical analysis techniques. Welter¹⁷ concluded that in combination with a baseline correction, the linearization of the raw absorption plot, Kubelka-Munk/modified Kubelka-Munk plot, or Tauc plot can provide a more consistent bandgap value; however, the knowledge regarding transition type is still needed in advance, and different features from mixture components are completely ignored. Another recent significant attempt to propose a unified methodology for bandgap energy determination was made by Zanatta. 16 The proposal suggested that the optical absorption coefficient, calculated from transmission/reflectance spectra, is fitted with the sigmoid-Boltzmann function before the bandgap energy can be determined from a simple formula. Although the justification for this fitting is purely empirical, the resulting bandgap values are greatly consistent with expected values with very low variance. This method also can provide some information regarding the disorder (order) of the material when Raman data are also available. Beside having the same drawback as other reported methods when being used for mixtures or materials with multiple features, this method also

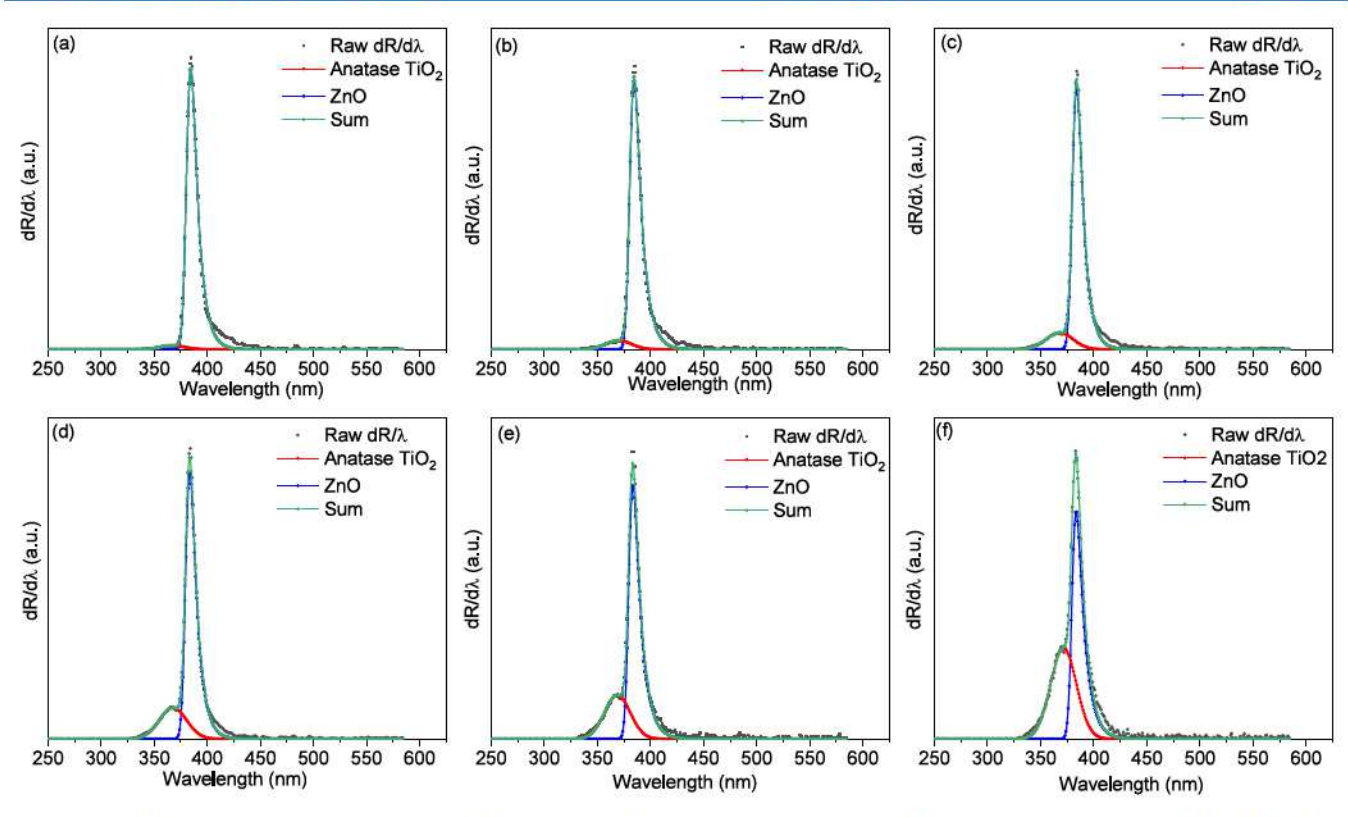
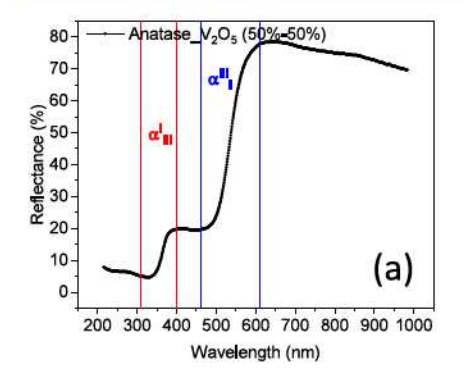


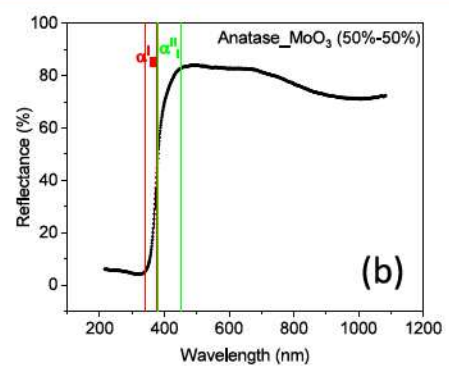
Figure 7. Peak deconvolution of anatase TiO₂ and ZnO mixtures with EMG function with nominal weight percent of TiO₂: (a) 12%, (b) 25%, (c) 40%, (d) 50%, (e) 60%, (f) 75%, and (g) 90%.

Table 3. Relative Response Factor of Binary Mixtures of Metal Oxides with Respect to Anatase TiO₂

metal oxide mixture with anatase ${\rm TiO_2}$	e relative response with respect to anatase TiO ₂		
TiO ₂ (rutile)	1.04		
TiO ₂ (brookite)	3.42		
CeO ₂	16		
ZnO	8.2		
SnO ₂	0.18		
V_2O_5	7.7		
MoO ₃	0.8		
Nb ₂ O ₅	1.36		
Ta_2O_5	0.036		
Y_2O_3	0.065		

suffers from the fitting point of view. Since the high-energy region of the absorption coefficient is usually irregular and noisy, 16 the criteria for fitting process using sigmoid-Boltzmann are considerably subjective, thus possibly leading to human errors. The sensitivity of UV-vis spectra analysis could be improved by taking the first derivative of raw spectra data. We previously presented the DPR method, 18 where the bandgap energies of anatase and rutile could be measured independently in the same sample of P25. Furthermore, the area under the deconvoluted derivative peaks represented the relative concentrations of the component solids in the mixture and were used to quantify composition. The technique was successfully implemented in situ during sample calcination and was used to track the onset of rutilization in the sample with temperature. Component identification in the DPR technique as reported had two assumptions: (1) peak deconvolution can





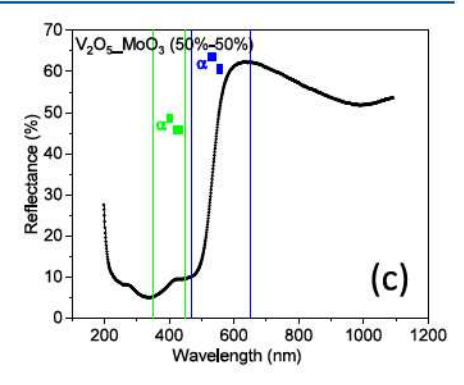


Figure 8. Raw reflectance spectra for 50%-50% mixtures of (a) anatase TiO_2 and V_2O_5 , (b) anatase TiO_2 and MoO_3 , and (c) V_2O_5 and MoO_3 . I: anatase TiO_2 . II: MoO_3 . III: V_2O_5 .

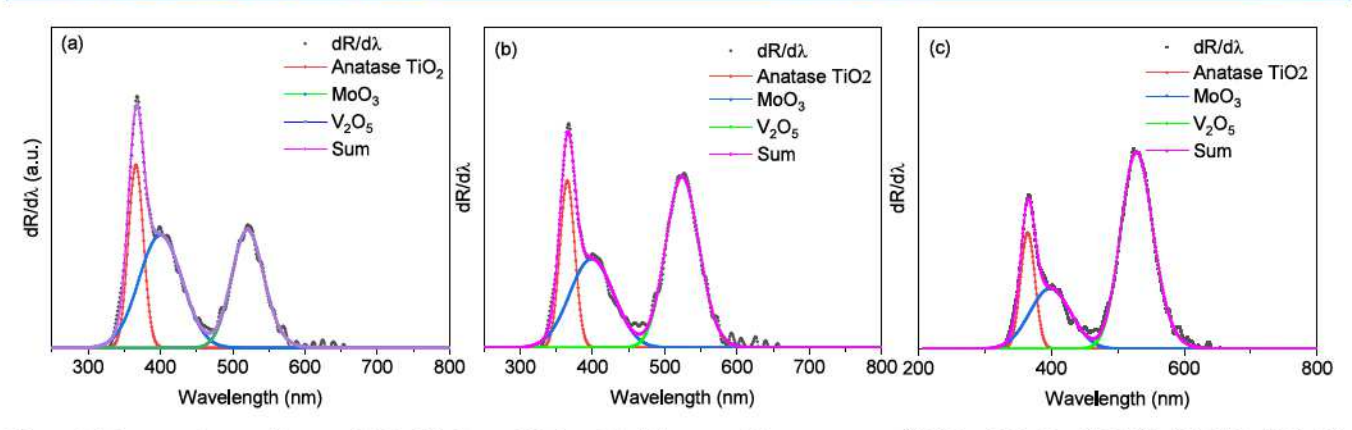


Figure 9. Ternary mixture of anatase TiO_2 , MoO_3 , and V_2O_5 with different weight percentages (% TiO_2 -% MoO_3 -% V_2O_5): (a) 11%-86%-3%, (b) 11%-84%-5%, and (c) 12%-77%-11%.

Table 4. Results of Phase Quantification Using DPR on Ternary Mixtures

sample	anatase TiO ₂		MoO ₃		V ₂ O ₅	
	nominal wt %	DPR wt %	nominal wt %	DPR wt %	nominal wt %	DPR wt %
1	11	14	86	80	3	6
2	11	14	84	76	5	10
3	12	15	77	69	11	16

be carried out by fitting Gaussian peaks so that each peak represents one (1) crystalline phase in the mixture, and (2) the peak position could correspond to the bandgap energy of the pure component. While the first assumption appears to hold for the case of anatase and rutile TiO_{2} , several other materials

seem not to follow. Figure 2a demonstrates a significant deviation between a single Gaussian function and the derivative spectrum of cerium oxide, and the peak maximum of the fitted function does not match the apparent maximum of the sample data. The low-energy tail extends further compared to the high-energy tail as well. While the fitting can be improved by adding additional Gaussian peaks, as shown in Figure 2b, now the second assumption would be violated since one pure material requires two distinct peaks, one of which has drastically different apparent bandgap energy. This violation eliminates the possibility of crystalline phase identification using a simple Gaussian function for cerium oxide.

3.3. EMG Function Fitting and Its Justification. The formula²⁰ for estimating the distribution or density of free electrons with respect to energy level:

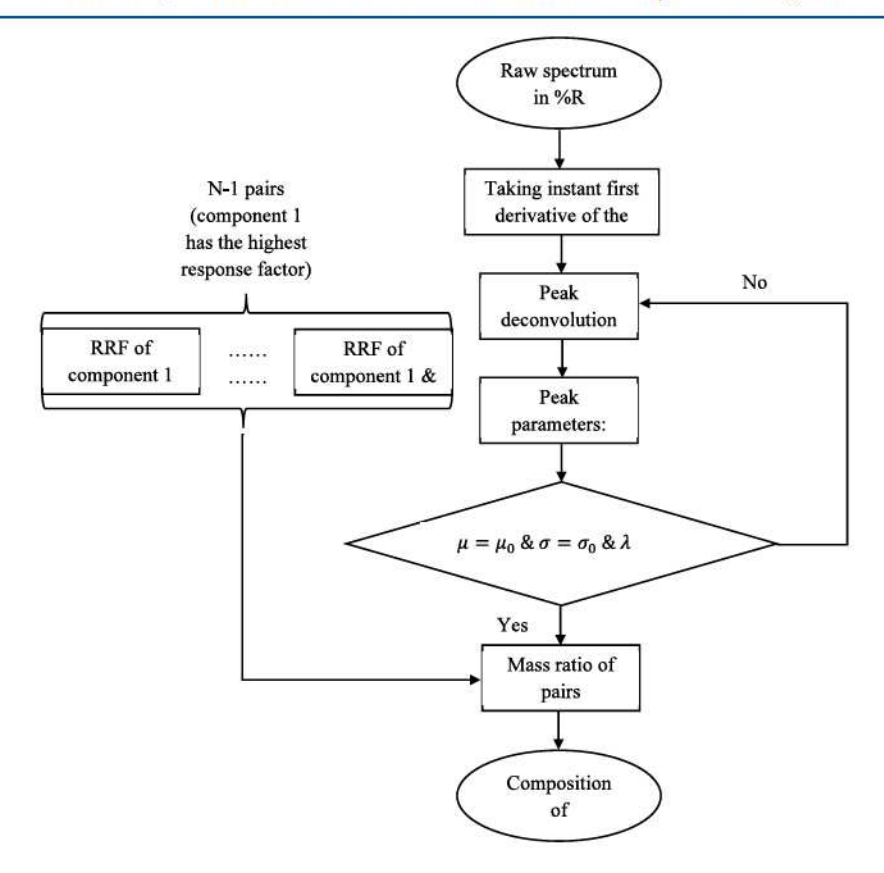


Figure 10. Stepwise technique of DPR quantification for mixtures of semiconductors.

$$n(E) = \int_{-\infty}^{+\infty} g(E) f(E) dE$$

Acknowledging that the probability of occupancy f(E) obeys the Fermi-Dirac distribution, the diverse electron distribution of materials in band-to-band transitions is caused mainly due to the unique band structure of these materials close to the bandgap region.

Figure 3 illustrates the shape of the electron density per unit energy as a result of the density of states and the corresponding occupancy probability. The mentioned formula also implies that the spectral intensity of excitation from a material due to photoinduction is expected to be peak-like. To account for various shapes of density of states and their effect in induced radiation, Gillespie et al. 40 introduced a list of possible models including monotonically decreasing models such as exponential, power law, and peak models, such as Gaussian, and its combination with other functions. In these models, only the Gaussian density of states combined with the Fermi-Dirac distribution results in symmetric density of charge carriers while others form a long tail in the low-energy regime. The Gaussian model for density of states has been rigorously derived for heavily doped semiconductors⁴¹ and then successfully used for organic materials, as reported by Qi and Wang. 42 The model was based on the fact that the central-limit theorem could be applied for both deep tail energy and longrange disorder. However, Halperin and Lax⁴³ argued that localization of states near the band edge change the underlying physics of the absorption behavior resulting in a change of scale for the absorption coefficient. Examples such as As₂S₃ spectra from photoconductivity experiments or ZnO spectra from electroreflectance⁴⁴ experiments showed significant asymmetry of the low-energy tail. The asymmetric peaks of these materials had linear exponential behavior in the lowenergy tail. The gradual change from Gaussian to linear exponential shape was shown by John⁴⁵ through mathematical consideration to be expectedly common among materials. This hints at the form of a fitting function which should be flexible enough to capture both the Gaussian behavior in the deep energy tail and linear exponential behavior in the shallow energy tail for the photoexcitation between valence and conduction bands.

Herein, we propose the use of the exponentially modified Gaussian distribution ⁴⁶ as an empirical fitting function for the spectral intensity of photoexcited phenomena which, in the scope of this study, is the derivative of UV-vis reflectance spectra:

$$f(x; A, \mu, \sigma, \lambda) = A \exp\left[\frac{\lambda}{2}(2\mu + \lambda\sigma^2 - 2x)\right] \operatorname{erfc}\left(\frac{\mu + \lambda\sigma^2 - x}{\sqrt{2}\sigma}\right)$$

where

$$\operatorname{erfc}(x) = 1 - \operatorname{erf}(x) = \frac{2}{\sqrt{\pi}} \int_{\pi}^{\infty} \exp(-t^2) dt$$

EMG is the result of convolution between Gaussian and exponential decay functions. Various forms of EMG have been widely used in the field of gas chromatography 47,48 to determine the retention time and peak area corresponding to different components in a gas mixture. Providing the characteristics of the electron distribution, the form of EMG was intentionally selected so that the exponential term only exhibits itself in the higher value of x, which will then be the wavelength in the fitting process. In the preceding expression,

 μ , $\sigma^2 > 0$, and $\lambda > 0$ are the peak position, variance of Gaussian component (full width at half-maximum, FWHM), and rate of exponential term ($\tau = 1/\lambda$ is usually called relaxation time, RT), respectively. The terminology relaxation time used in this work came from the conventional use in chromatography and mathematics and should be not be confused to relaxation time in dynamics of inelastic vibration. The chosen form of the EMG function has its peak fall on the side of Gaussian component, and its skewness could be determined as $\frac{2}{\sigma^3 \lambda^3} \Big(1 + \frac{1}{\sigma^2 \lambda^2}\Big)^{-3/2}.$ As the $\frac{\tau}{\sigma}$ ratio approaches zero, the function becomes asymptotically Gaussian.

Before moving into demonstrating applications of EMG peak fitting for DPR, it is worth noticing that the first derivative of diffuse reflectance spectra could be expected to possess similar features to peaks in electroreflectance 44,50 and photoconductivity⁵¹ spectra in the vicinity of the bandgap region. Excitons, for instance, are not electrically conductive and are silent in the photoconductivity experiments and could affect the absorption features in the UV-vis spectra. However, near the edge of the density of states, the band-to-band transition could still safely be assumed to dominate the observed phenomena. Additionally, the focus of this study on the derivative of the UV-vis spectrum originates from the 2fold advantage of this form. Taking derivatives of the reflectance can considerably enhance the sensitivity of the analysis especially for materials or mixtures with more subtler features. Likewise, as quickly mentioned above, the peak-like feature of each semiconductor can be described as the distribution of electrons at different energy levels within the valence band that are excited during the experiments. Such a consideration lays the foundation for the use of peak area to quantify the contribution of component semiconductors in the mixture.

Last but not least, even though Kubelka—Munk function has been widely used to analyze the UV—vis spectra, as the function was developed to approximate the absorption coefficient, ⁵² this approximation, which is strictly a mathematical artifice, ⁵³ has been reported to fail when the materials exhibit considerable absorbance at low energy. ^{53,54} In this work, we elect the use of derivative of raw reflectance, which is shown to provide comparable bandgap energies in the literature, ¹⁷ to leverage on the sensitivity enhancement by the taking the derivative of the spectra without significantly reduce the signal-to-noise ratio due to multiple mathematical transformation.

3.4. DPR for Pure Materials. Table 1 summarizes the parameters obtained from fitting an EMG function to each pure material. In application of anatase and rutile TiO2, Pennington¹⁸ mentioned that component identity in DPR using a Gaussian function could be via peak position. Peaks of metal oxides such as rutile TiO2 (400 nm), Nb2O5 (396 nm), and MoO₃ (406 nm) or CeO₂ (382 nm) and ZnO (381 nm) nevertheless are in proximity. Beside peak position μ , the EMG function provides the half-width at half-maximum (HWHM) of the high-energy tail $(\sigma^2/2)$ and RT of the low-energy tail $(1/\lambda)$ as two other parameters that are useful in peak identification. These parameters, which lend sensitivity to the method analysis, can be considered as a representation of the particular band structure at the band edge of semiconductors. These parameters of component semiconductors in mixtures are supposed to be constant or negligibly deviating from those

of pure components. This observation will be shown below in this work.

It has been shown that peaks from photoconductivity experiments could be used to determine bandgap energy. This quick technique was then verified²⁹ to give error within 0.1 eV compared to other techniques. Table 2 illustrates both BGE determined from the Tauc method and BGE as peak position (μ) of EMG. Most of these values differ within 0.1 eV. It is noticeable that BGE values obtained from DPR of UVvisible spectroscopy seem to be larger than those found by Tauc. Similar behavior was also observed previously when absorption energy determined from photoconductivity analysis^{29,70} was compared to that from the Tauc method. Extrapolation of a tangent line in the Tauc plot was meant to find the highest valence band occupied by electrons that are potentially photoinduced free charge carriers. This follows the strict definition of bandgap energy in crystalline materials, which shows use in the field of electronics. In comparison, the peak from DPR of UV-vis spectroscopy or photoconductivity could be interpreted as the energy level where electron density is highest in reference to the conduction band. Also, there is an efficiency for the incident photons to generate excitons from the valence band. This implies that in the DPR analysis, the peak-shape curve could be interpreted as the distribution of excited electrons from different energy states in the valence band with the peak position representing the effective bandgap energy. As a result, the effective BGE determined by DPR provides more suitable information for the field of photocatalysis.

Among the listed pure materials, brookite TiO_2 , CeO_2 , and ZnO have the highest skewness values of 63.86, 47.46, and 145.40, respectively. As expected from DPR analysis using the EMG function, shown in Figure 4, these materials exhibited significantly asymmetric peaks. The strong effect of the exponential behavior from the low-energy tail of these materials was the cause of difficulties in finding the tangent line while using the Tauc method. Furthermore, similar to the Tauc method, DPR proved to be applicable regardless the position of the bandgap position, such as CuO with 1.43 eV or Y_2O_3 with 5.68 eV, as long as it is within the range of UV—visible to near-infrared red spectrum.

3.5. Component Quantification in Binary Mixtures. Figure 5 demonstrates peak deconvolutions of DPR for mixtures of anatase TiO2 and MoO3 with different component concentrations. Peak identities, including peak position μ , HWHM of the Gaussian component $(\sigma^2/2)$, and RT of the exponential component $(1/\lambda)$, for these mixtures only varied negligibly as listed in Table 2. The pairwise value of RRF was obtained by minimizing the R2 with pair RRF as parameter in linear regression of calculated weight percentage on nominal weight percentage as shown in Figure 6. For mixtures of anatase TiO2 and MoO3, the RRF was found to be 0.8, implying that the light absorption of MoO3 was more intense in these mixtures. The RRF value reported in this work for the pair of anatase and rutile TiO2 is 1.04, an update from the RRF value reported using simple Gaussian functions. 18 Besides, it is important to note that although the characteristic fitting parameters obtained from pure material analysis, in principle, can be used to identify components in an arbitrary physical mixture, changes in some physiochemical properties such as morphologies or surface area might have some effects on those fitting parameters that represent pure component metal oxides. Previous work on the DPR method with Gaussian fitting

function¹⁸ has shown that the change of aggregate size by grinding treatment, which was also used in our work, has a negligible effect on the fitting process and identification of components. Comprehensively tackling the effects of other physiochemical properties would bring forth further applications of DPR analysis but would also require a separate systematic investigation beyond the scope of this work.

It should be noted that for mixtures in which BGEs are in proximity, the RT of the high-energy peak and/or HWHM of the low-energy peak has to be fixed during deconvolution to achieve reasonable values for the rest of the important peak parameters. This requirement emerged as a trade-off for flexibility of the EMG function. However, as one parameter was fixed, other parameters were obtained spontaneously from the fitting procedure. Peak deconvolution and linear regression of DPR for binary mixtures of anatase TiO₂ and ZnO, as in Figure 7, demonstrated the capability of the technique to identify vicinal peaks. A similar analysis technique was applied to other binary mixtures in which anatase TiO₂ was one of the components; pairwise RRF values are reported in Table 3.

In different environments, the response factors of a single semiconductor could be significantly different. As demonstrated by Figure 8, raw data were collected as reflectance percentage. The magnitude of change of reflectance in the bandgap energy region of a component directly corresponds to the area of its representative peak after taking the first derivative. It could be observed that for binary mixtures (I and II), in the peak region of component I, its reflectance is affected by its own light absorption and component II's absorption, and vice versa. This light reflectance response interaction was manifested in the percentage of component peaks in such a way that at 50%-50% (wt %-wt %) mixture, the peak area ratio is no more than 1:1. Introducing pairwise relative response factors could resolve this problem. However, as stated, in order to determine compositions in pairs of semiconductors (i and j), the effect of absorption of i in the peak region of j relative to the effect of absorption of j in the peak region of i has to be known. In other words, for a system of three semiconductors, by using relative response factors of two pairs (TiO₂ and V₂O₅; TiO₂ and MoO₃), one is not able to obtain the relative response factor of the last pair (MoO₃ and V_2O_5).

$$\frac{RRF_{M_0O_3/Ana-TiO_2}}{RRF_{V_2O_5/Ana-TiO_2}} = 0.11 \neq RRF_{M_0O_3/V_2O_5} = 0.07$$

This problem could be attributed to the loss of information since the raw percentage of reflectance does not provide enough information to derive an absolute response factor for pure materials. However, it could be reasoned that when a material A with significantly high response factors is only present in a small amount, compared to other materials (B_1 , B_2 , ...) with low response factors, the aforementioned interaction between RRF_{B1/A}, RRF_{B2/A}, ... could be neglected. As a result, available RRF values with respect to the materials, having the highest response factor, could be used to quantify phase components.

3.6. Component Quantification in Ternary Mixtures. Ternary mixtures of metal oxides of anatase ${\rm TiO}_2$, ${\rm MoO}_3$, and ${\rm V}_2{\rm O}_5$ were also made and compositionally quantified by using DPR with previously found pairwise RRF values. Figure 9 and Table 4 show the results of applying DPR to ternary mixtures. Since peaks representing components in mixtures hold the

1

same peak parameters as pure materials, each component could be identified, and its composition could be estimated. In the tested samples, vanadium oxide, which has the highest response factor, only comprised a small amount and thus satisfied the required premise for multicomponent quantification process using the DPR method. By using relative response factor of anatase and molybdenum with respect to vanadium, composition of three metal oxide phases could be obtained. This method showed very high sensitivity for those materials with strong light response. It seemed that this analysis could be extended to more components in higher-order mixtures with acceptable accuracy if their peaks and relevant characteristics could be identified. Figure 10 shows a stepwise method that could be implemented as a code to quantify components in a semiconductor mixture. After taking the first derivative of the raw reflectance spectrum, the resulting data is deconvoluted using EMG functions in such a way that each peak should carry its parameters which match known pure component peaks with some tolerance. Then, N-1 pairwise response factors, in an N-component mixture, could be used to find the mass or molar ratio between each pair. The final weight or molar percentage of each component could then be calculated from these pairwise mass ratios.

4. CONCLUSIONS

DPR UV—vis spectroscopy with a Gaussian fitting function was revised and modified by implementation of the EMG as a fitting function and λ as a function parameter to represent the low-energy tail of the UV—vis spectra. Although the fitting function was not mathematically derived from a theoretical viewpoint, similarity between the asymmetric energy distribution of electronic excitation and the EMG function was demonstrated from a physical perspective.

Application of the DPR method with the EMG fitting function in bandgap energy determination extended the applicability of the method to all phases of titanium oxide and many catalytically interesting materials including CeO₂, ZnO, SnO₂, V₂O₅, MoO₃, Y₂O₃, Ta₂O₅, and Nb₂O₅. The DPR method showed a low susceptibility to subjective error and decent sensitivity, which offered an identification method for individual component materials via peak characteristics, intrinsically belonging to distinct metal oxide phases, in various mixtures. Response factors, which could be generally applied to quantify metal oxide composition, irrespective of the specific UV—vis spectrometer, were collected. Generalization of the DPR UV—vis phase quantification for ternary mixtures was demonstrated to be feasible by using response factors obtained from binary mixtures.

ASSOCIATED CONTENT

Supporting Information

The Supporting Information is available free of charge at https://pubs.acs.org/doi/10.1021/acs.jpcc.4c03763.

Raw reflectance, Tauc analysis, DPR analysis with EMG for of pure anatase TiO_2 , rutile TiO_2 , brookite TiO_2 , CeO_2 , ZnO, CuO, SnO_2 , V_2O_5 , MoO_3 , Nb_2O_5 , Ta_2O_5 , and Y_2O_3 ; raw reflectance spectra of anatase TiO_2 and V_2O_5 binary mixtures; DPR analysis with EMG for anatase TiO_2 and V_2O_5 binary mixtures; calculated weight percentage, obtained from regressed RRF, versus nominal weight percentage of anatase TiO_2 in binary mixture with V_2O_5 ; DPR analysis with EMG for anatase

TiO2 and ZnO binary mixtures; calculated weight percentage, obtained from regressed RRF, versus nominal weight percentage of anatase TiO2 in binary mixture with ZnO; raw reflectance spectra of anatase TiO2 and MoO3 binary mixtures; DPR analysis with EMG for anatase TiO2 and MoO3 binary mixtures; calculated weight percentage, obtained from regressed RRF, versus nominal weight percentage of anatase TiO2 in binary mixture with MoO3; raw reflectance spectra of anatase TiO2 and Nb2O5 binary mixtures; DPR analysis with EMG for anatase TiO₂ and Nb₂O₅ binary mixtures; calculated weight percentage, obtained from regressed RRF, versus nominal weight percentage of anatase TiO2 in binary mixture with Nb2O5; raw reflectance spectra of anatase TiO2 and brookite TiO2 binary mixtures; DPR analysis with EMG for anatase TiO2 and brookite TiO2 binary mixtures; calculated weight percentage, obtained from regressed RRF, versus nominal weight percentage of anatase TiO2 in binary mixture with brookite TiO2; raw reflectance spectra of anatase TiO2 and Ta2O5 binary mixtures; DPR analysis with EMG for anatase TiO2 and Ta2O5 binary mixtures; calculated weight percentage, obtained from regressed RRF, versus nominal weight percentage of anatase TiO2 in binary mixture with Ta2O5; raw reflectance spectra of anatase TiO2 and SnO2 binary mixtures; DPR analysis with EMG for anatase TiO2 and SnO2 binary mixtures; calculated weight percentage, obtained from regressed RRF, versus nominal weight percentage of anatase TiO2 in binary mixture with SnO2; raw reflectance spectra of anatase TiO2 and Y2O3 binary mixtures; DPR analysis with EMG for anatase TiO₂ and Y₂O₃ binary mixtures; calculated weight percentage, obtained from regressed RRF, versus nominal weight percentage of anatase TiO2 in binary mixture with Y2O3; raw reflectance spectra of anatase TiO2 and CeO2 binary mixtures; DPR analysis with EMG for anatase TiO2 and CeO2 binary mixtures; calculated weight percentage, obtained from regressed RRF, versus nominal weight percentage of anatase TiO₂ in binary mixture with CeO2 (PDF)

AUTHOR INFORMATION

Corresponding Author

Fuat E. Celik – Department of Chemical and Biochemical Engineering Rutgers, The State University of New Jersey, Piscataway, New Jersey 08854, United States; oorcid.org/0000-0002-5891-6375; Email: fuat.celik@rutgers.edu

Authors

Thu D. Nguyen — Department of Chemical and Biochemical Engineering Rutgers, The State University of New Jersey, Piscataway, New Jersey 08854, United States

Chenfeng Huang – Department of Chemical and Biochemical Engineering Rutgers, The State University of New Jersey, Piscataway, New Jersey 08854, United States

George Tsilomelekis — Department of Chemical and Biochemical Engineering Rutgers, The State University of New Jersey, Piscataway, New Jersey 08854, United States; orcid.org/0000-0002-0435-8216

Complete contact information is available at: https://pubs.acs.org/10.1021/acs.jpcc.4c03763

Notes

The authors declare no competing financial interest.

ACKNOWLEDGMENTS

This work was supported by the National Science Foundation (CBET 1751683) and in part by Rutgers, The State University of New Jersey. The authors also thank Dr. Ashley M. Pennington for her contributions to the DPR method and advice throughout this project.

REFERENCES

- (1) Cheng, W.-H. Methanol and Formaldehyde Oxidation Study over Molybdenum Oxide. J. Catal. 1996, 158 (2), 477–485.
- (2) Sattler, J. J. H. B.; Ruiz-Martinez, J.; Santillan-Jimenez, E.; Weckhuysen, B. M. Catalytic Dehydrogenation of Light Alkanes on Metals and Metal Oxides. *Chem. Rev.* 2014, 114 (20), 10613–10653.
- (3) Martínez-Huerta, M. V.; Gao, X.; Tian, H.; Wachs, I. E.; Fierro, J. L. G.; Bañares, M. A. Oxidative dehydrogenation of ethane to ethylene over alumina-supported vanadium oxide catalysts: Relationship between molecular structures and chemical reactivity. *Catal. Today* 2006, 118 (3), 279–287.
- (4) Chen, K.; Bell, A. T.; Iglesia, E. Kinetics and Mechanism of Oxidative Dehydrogenation of Propane on Vanadium, Molybdenum, and Tungsten Oxides. *J. Phys. Chem. B* 2000, 104 (6), 1292–1299.
- (5) Nguyen, T. D.; Zheng, W.; Celik, F. E.; Tsilomelekis, G. CO₂-assisted ethane oxidative dehydrogenation over MoOx catalysts supported on reducible CeO₂-TiO₂. Catalysis Science & Technology 2021, 11 (17), 5791-5801.
- (6) Palma, V.; Barba, D. Vanadium-ceria catalysts for H2S abatement from biogas to feed to MCFC. *Int. J. Hydrogen Energy* 2017, 42 (3), 1891–1898.
- (7) Rousseau, R.; Dixon, D. A.; Kay, B. D.; Dohnálek, Z. Dehydration, dehydrogenation, and condensation of alcohols on supported oxide catalysts based on cyclic (WO3)3 and (MoO3)3 clusters. *Chem. Soc. Rev.* 2014, 43 (22), 7664–7680.
- (8) Tsilomelekis, G.; Boghosian, S. An operando Raman study of molecular structure and reactivity of molybdenum(vi) oxide supported on anatase for the oxidative dehydrogenation of ethane. *Phys. Chem. Phys.* 2012, 14 (7), 2216–2228.
- (9) Lee, K. M.; Lai, C. W.; Ngai, K. S.; Juan, J. C. Recent developments of zinc oxide based photocatalyst in water treatment technology: A review. *Water Res.* 2016, 88, 428-448.
- (10) Channei, D.; Inceesungvorn, B.; Wetchakun, N.; Ukritnukun, S.; Nattestad, A.; Chen, J.; Phanichphant, S. Photocatalytic Degradation of Methyl Orange by CeO₂ and Fe-doped CeO₂ Films under Visible Light Irradiation. Sci. Rep. 2014, 4 (1), 5757.
- (11) Schneider, J.; Matsuoka, M.; Takeuchi, M.; Zhang, J.; Horiuchi, Y.; Anpo, M.; Bahnemann, D. W. Understanding TiO₂ Photocatalysis: Mechanisms and Materials. *Chem. Rev.* **2014**, *114* (19), 9919–9986.
- (12) Tauc, J.; Grigorovici, R.; Vancu, A. Optical Properties and Electronic Structure of Amorphous Germanium. *physica status solidi* (b) 1966, 15 (2), 627-637.
- (13) Trejo-Tzab, R.; Alvarado-Gil, J. J.; Quintana, P. Photocatalytic Activity of Degussa P25 TiO₂/Au Obtained Using Argon (Ar) and Nitrogen (N2) Plasma. *Top. Catal.* 2011, 54 (1), 250–256.
- (14) Luttrell, T.; Halpegamage, S.; Tao, J.; Kramer, A.; Sutter, E.; Batzill, M. Why is anatase a better photocatalyst than rutile? Model studies on epitaxial TiO₂ films. Sci. Rep. 2014, 4 (1), 4043.
- (15) Viezbicke, B. D.; Patel, S.; Davis, B. E.; Birnie, D. P. Evaluation of the Tauc method for optical absorption edge determination: ZnO thin films as a model system. *Physica Status Solidi* (b) 2015, 252 (8), 1700–1710.
- (16) Zanatta, A. R. Revisiting the optical bandgap of semiconductors and the proposal of a unified methodology to its determination. *Sci. Rep* 2019, 9 (1), 11225.
- (17) Welter, E. S.; Garg, S.; Gläser, R.; Goepel, M. Methodological Investigation of the Band Gap Determination of Solid Semi-

- conductors via UV/Vis Spectroscopy. ChemPhotoChem. 2023, 7 (6), 2367-0932.
- (18) Pennington, A. M.; Okonmah, A. I.; Munoz, D. T.; Tsilomelekis, G.; Celik, F. E. Changes in Polymorph Composition in P25-TiO₂ during Pretreatment Analyzed by Differential Diffuse Reflectance Spectral Analysis. *J. Phys. Chem. C* 2018, 122 (9), 5093—5104
- (19) Wojdyr, M. Fityk: a general-purpose peak fitting program. J. Appl. Crystallogr. 2010, 43 (5-1), 1126-1128.
- (20) Ashcroft, N. W.; Mermin, N. D. Solid State Physics. Cengage, 2021; pp 132-150.
- (21) Urbach, F. The Long-Wavelength Edge of Photographic Sensitivity and of the Electronic Absorption of Solids. *Phys. Rev.* 1953, 92 (5), 1324–1324.
- (22) Dow, J. D.; Redfield, D. Toward a Unified Theory of Urbach's Rule and Exponential Absorption Edges. *Phys. Rev. B* 1972, 5 (2), 594-610.
- (23) Redfield, D. Effect of Defect Fields on the Optical Absorption Edge. *Phys. Rev.* 1963, 130 (3), 916–918.
- (24) Sumi, H.; Toyozawa, Y. Urbach-Martienseen Rule and Exciton Trapped Momentarily by Lattice Vibrations. *J. Phys. Soc. Jpn.* 1971, 31 (2), 342–358.
- (25) Szczyrbowski, J. The Exponential Shape of the Optical Absorption Edge Tail. *physica status solidi* (b) 1981, 105 (2), 515–524.
- (26) Cody, G. D. Urbach edge of crystalline and amorphous silicon: a personal review. J. Non-Cryst. Solids 1992, 141, 3-15.
- (27) Skumanich, A.; Frova, A.; Amer, N. M. Urbach tail and gap states in hydrogenated a-SiC and a-SiGe alloys. *Solid State Commun.* 1985, 54 (7), 597–601.
- (28) Tauc, J. Optical properties and electronic structure of amorphous Ge and Si. Mater. Res. Bull. 1968, 3 (1), 37-46.
- (29) Davis, E. A.; Mott, N. F. Conduction in non-crystalline systems V. Conductivity, optical absorption and photoconductivity in amorphous semiconductors. *Philosophical Magazine: A Journal of Theoretical Experimental and Applied Physics* 1970, 22 (179), 0903–
- (30) Mott, N. F.; Davis, E. A. Electronic Processes in Non-Crystalline Materials; OUP: Oxford, 2012; pp 199-314.
- (31) Dawson, R. M.; Li, Y. M.; Gunes, M.; Heller, D.; Nag, S.; Collins, R. W.; Wronski, C. R.; Bennett, M.; Li, Y. M. Optical Properties of Hydrogenated Amorphous Silicon, Silicon-Germanium and Silicon-Carbon Thin Films. MRS Online Proceedings Library 1992, 258 (1), 595–600.
- (32) Sweenor, D. E.; O'Leary, S. K.; Foutz, B. E. On defining the optical gap of an amorphous semiconductor: an empirical calibration for the case of hydrogenated amorphous silicon. *Solid State Commun.* 1999, 110 (5), 281–286.
- (33) Yoshino, Y.; Makino, T.; Katayama, Y.; Hata, T. Optimization of zinc oxide thin film for surface acoustic wave filters by radio frequency sputtering. *Vacuum* 2000, 59 (2), 538–545.
- (34) Abb, M.; Sepúlveda, B.; Chong, H. M. H.; Muskens, O. L. Transparent conducting oxides for active hybrid metamaterial devices. *Journal of Optics* 2012, 14 (11), 114007.
- (35) Kumar, B. R.; Rao, T. Influence of sputtering power on physical properties of nanostructured Zinc Aluminum Oxide thin films for photovoltaic applications. *Dig. J. Nanomater. Biostruct.* **2012**, 7 (3), 1051–1061.
- (36) Biswas, P.; Kundu, S.; Banerji, P.; Bhunia, S. Super rapid response of humidity sensor based on MOCVD grown ZnO nanotips array. Sens. Actuators, B 2013, 178, 331–338.
- (37) Chithambararaj, A.; Bose, A. C. Hydrothermal synthesis of hexagonal and orthorhombic MoO3 nanoparticles. *J. Alloys Compd.* 2011, 509 (31), 8105–8110.
- (38) Bouzidi, A.; Benramdane, N.; Tabet-Derraz, H.; Mathieu, C.; Khelifa, B.; Desfeux, R. Effect of substrate temperature on the structural and optical properties of MoO3 thin films prepared by spray pyrolysis technique. *Materials Science and Engineering: B* 2003, 97 (1), 5–8.

- (39) Coulter, J. B.; Birnie, D. P. Assessing Tauc Plot Slope Quantification: ZnO Thin Films as a Model System. *physica status solidi (b)* 2018, 255 (3), 1700393.
- (40) Jodie Corbridge Gillespie, J. D. a. A. M. S. Density of State Models and Temperature Dependence of Radiation Induced Conductivity. In *Proceedings of the 13th Spacecraft Charging Technology Conference*, 2014; p 8.
- (41) Kane, E. O. Thomas-Fermi Approach to Impure Semiconductor Band Structure. *Phys. Rev.* 1963, 131 (1), 79–88.
- (42) Qi, B.; Wang, J. Open-circuit voltage in organic solar cells. J. Mater. Chem. 2012, 22 (46), 24315-24325.
- (43) Halperin, B. I.; Lax, M. Impurity-Band Tails in the High-Density Limit. I. Minimum Counting Methods. *Phys. Rev.* 1966, 148 (2), 722-740.
- (44) Seraphin, B. O. Electroreflectance and the semiconductor surface. Surf. Sci. 1969, 13 (1), 136-150.
- (45) John, S.; Soukoulis, C.; Cohen, M. H.; Economou, E. N. Theory of Electron Band Tails and the Urbach Optical-Absorption Edge. *Phys. Rev. Lett.* 1986, *57* (14), 1777–1780.
- (46) Grushka, E. Characterization of exponentially modified Gaussian peaks in chromatography. *Anal. Chem.* 1972, 44 (11), 1733–1738.
- (47) Kalambet, Y.; Kozmin, Y.; Mikhailova, K.; Nagaev, I.; Tikhonov, P. Reconstruction of chromatographic peaks using the exponentially modified Gaussian function. *Journal of Chemometrics* 2011, 25 (7), 352–356.
- (48) Dyson, N. Chromatographic Integration Methods, 2nd ed.; The Royal Society of Chemistry: 1998; pp 12-23.
- (49) Ibach, H.; Lüth, H. Solid-State Physics: An Introduction to Principles of Materials Science; with 100 Problems; Springer: 2003; pp 159-189.
- (50) Cerdeira, F.; Cardona, M. Photoreflectance and electroreflectance in silicon. Solid State Commun. 1969, 7 (12), 879-882.
- (51) Wieting, T. J.; Yoffe, A. D. Excitons and Photoconductivity in Transition-Metal Dichalcogenides. *physica status solidi* (b) 1970, 37 (1), 353–366.
- (52) Kubelka, P. New Contributions to the Optics of Intensely Light-Scattering Materials. *Part I. J. Opt. Soc. Am.* 1948, 38 (5), 448–457.
- (53) Torrent, J.; Barrón, V. Diffuse Reflectance Spectroscopy. In *Methods of Soil Analysis Part 5—Mineralogical Methods*; SSSA Book Series: 2008; pp 367–385.
- (54) Makuła, P.; Pacia, M.; Macyk, W. How To Correctly Determine the Band Gap Energy of Modified Semiconductor Photocatalysts Based on UV-Vis Spectra. *J. Phys. Chem. Lett.* 2018, 9 (23), 6814–6817
- (55) Mattsson, A.; Österlund, L. Adsorption and Photoinduced Decomposition of Acetone and Acetic Acid on Anatase, Brookite, and Rutile TiO₂ Nanoparticles. *J. Phys. Chem. C* 2010, 114 (33), 14121–14132.
- (56) Khan, M. M.; Ansari, S. A.; Pradhan, D.; Han, D. H.; Lee, J.; Cho, M. H. Defect-Induced Band Gap Narrowed CeO₂ Nanostructures for Visible Light Activities. *Ind. Eng. Chem. Res.* 2014, 53 (23), 9754–9763.
- (57) Thomas, D. G. The exciton spectrum of zinc oxide. J. Phys. Chem. Solids 1960, 15 (1), 86-96.
- (58) Srikant, V.; Clarke, D. R. On the optical band gap of zinc oxide. J. Appl. Phys. 1998, 83 (10), 5447–5451.
- (59) Jellison, G. E.; Boatner, L. A. Optical functions of uniaxial ZnO determined by generalized ellipsometry. *Phys. Rev. B* 1998, 58 (7), 3586–3589.
- (60) Koffyberg, F. P.; Benko, F. A. A photoelectrochemical determination of the position of the conduction and valence band edges of p-type CuO. *J. Appl. Phys.* 1982, 53 (2), 1173–1177.
- (61) Ghijsen, J.; Tjeng, L. H.; van Elp, J.; Eskes, H.; Westerink, J.; Sawatzky, G. A.; Czyzyk, M. T. Electronic structure of Cu₂O and CuO. Phys. Rev. B 1988, 38 (16), 11322–11330.

- (62) Gu, F.; Wang, S. F.; Lü, M. K.; Zhou, G. J.; Xu, D.; Yuan, D. R. Photoluminescence Properties of SnO₂ Nanoparticles Synthesized by Sol-Gel Method. *J. Phys. Chem. B* 2004, 108 (24), 8119–8123.
- (63) Ahmed, A. S.; Shafeeq, M. M.; Singla, M. L.; Tabassum, S.; Naqvi, A. H.; Azam, A. Band gap narrowing and fluorescence properties of nickel doped SnO₂ nanoparticles. *J. Lumin.* 2011, 131 (1), 1–6.
- (64) Jiang, H.; Nagai, M.; Kobayashi, K. Enhanced photocatalytic activity for degradation of methylene blue over V2O5/BiVO4 composite. *J. Alloys Compd.* 2009, 479 (1), 821–827.
- (65) Chen, X.; Yu, T.; Fan, X.; Zhang, H.; Li, Z.; Ye, J.; Zou, Z. Enhanced activity of mesoporous Nb2O5 for photocatalytic hydrogen production. *Appl. Surf. Sci.* 2007, 253 (20), 8500–8506.
- (66) Chun, W.-J.; Ishikawa, A.; Fujisawa, H.; Takata, T.; Kondo, J. N.; Hara, M.; Kawai, M.; Matsumoto, Y.; Domen, K. Conduction and Valence Band Positions of Ta2OS, TaON, and Ta3NS by UPS and Electrochemical Methods. J. Phys. Chem. B 2003, 107 (8), 1798–1803
- (67) Morikawa, T.; Saeki, S.; Suzuki, T.; Kajino, T.; Motohiro, T. Dual functional modification by N doping of Ta2O5: p-type conduction in visible-light-activated N-doped Ta2O5. *Appl. Phys. Lett.* 2010, 96 (14), 142111.
- (68) Guo, H.; Zhang, W.; Lou, L.; Brioude, A.; Mugnier, J. Structure and optical properties of rare earth doped Y2O3 waveguide films derived by sol-gel process. *Thin Solid Films* 2004, 458 (1), 274–280.
- (69) Robertson, J. Band offsets of wide-band-gap oxides and implications for future electronic devices. Journal of Vacuum Science & Technology B: Microelectronics and Nanometer Structures Processing, Measurement, and Phenomena 2000, 18 (3), 1785–1791.
- (70) Davis, E. A.; Shaw, R. F. Characteristic phenomena in amorphous semiconductors. J. Non-Cryst. Solids 1970, 2, 406-431.